THE JOURNAL OF PHYSICAL CHEMISTRY C

Article

pubs.acs.org/JPCC

Impact of Structure and Composition on the Dealloying of $Cu_xAu_{(1-x)}$ Bulk and Nanoscale Alloys

Jiaxin Xia,[†] Stephen Ambrozik,[†] Cameron C. Crane,[‡] Jingyi Chen,[‡] and Nikolay Dimitrov*[,†]

[†]Department of Chemistry, SUNY at Binghamton, PO Box 6000, Binghamton, New York 13902, United States

[‡]Department of Chemistry and Biochemistry, University of Arkansas, Fayetteville, Arkansas 72701, United States

ABSTRACT: In this work, the impact of structure and composition on the dealloying of bulk and nanoscale alloys $Cu_xAu_{(1-x)}$ have been discussed. In comparison with the dealloying of Ag—Au alloys, the Cu—Au system exhibits dealloying curves with more features associated generally with multistage dealloying. It has been shown for the first time that three stages exist during dealloying process of bulk $Cu_xAu_{(1-x)}$ (x = 0.7 and 0.8) alloys. The dealloying critical potential, E_c, has been associated with the starting point of stage II in which the anodic current slowly increases. Analysis of data from this work along with results of others suggests a monotonic potential dependence of E_c upon the composition of bulk $Cu_xAu_{(1-x)}$ alloys in the range of x from 0.70 to 0.95. The dealloying behavior of $Cu_{0.75}Au_{0.25}$ (Cu_3Au) intermetallic (length ~19 nm, width ~10 nm) and random alloy (length ~23 nm, width ~9 nm) nanorods have also been discussed. Very close values of E_c have been determined for both types of nanorods with the random alloy dealloying at slightly more negative potentials (c.a. 15−20 mV) than the intermetallic. In addition, both Cu_3Au nanorods feature close to 200 mV lower E_c than bulk alloys with identical composition. Formic acid oxidation tests reveal that the catalysts generated by platinization of as-synthesized and dealloyed nanorods exhibit very good activity with peak current densities in the range of 3.5 to 5.5 mA.cm^{-2}. Both catalysts withstand testing of more than 1500 cycles. Overall, the results of this study demonstrate unique aspects of $Cu_xAu_{(1-x)}$ dealloying and ascertain the feasibility of nanosized frameworks (dealloyed structures or nanoparticles) as catalyst supports in fuel cell applications.

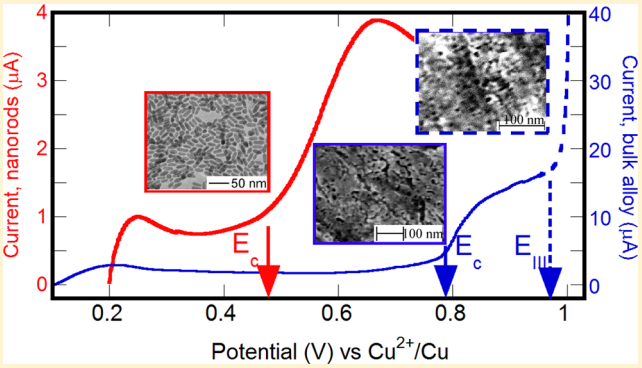

1. INTRODUCTION

The development of efficient catalysts, mostly involving platinum is very important in modern fuel cells. Platinum is highly efficient at catalyzing fuel cell reactions, but the high cost of platinum calls for limited use of the material in order to maximize device feasibility. In order to minimize the usage of Pt and expose maximum surface area of the catalyst to the solution, the catalyst has been made rough and porous. Nowadays, commonly nanoparticles (NPs) are chosen as catalysts and/or support material due to their naturally large surface area-to-volume ratio and different physical and chemical properties. Another good candidate for Pt support is nanoporous Au (NPG).[1] NPG is a material with continuous Au structure featuring interconnected nanosized pores and ligaments, this conductive material has an open, 3D porous framework with surface areas that even in ultrathin NPG layer configuration are tens to hundreds of times larger than the area of planar Au.[2−4] The NPG can be further functionalized with Pt by surface-limited redox replacement (SLRR) to form Pt-NPG. This Pt-NPG can then be further applied as a catalyst for the formic acid oxidation reaction.[5]

In our previous work, an all-electrochemical approach has been introduced as an alternative to NPs for developing catalysts for fuel-cell applications.[5] In this approach, by the electrodeposition of a $Au_xAg_{(1-x)}$ thin film (TF) on Au or glassy carbon (GC) substrate, and then selective electrochemical dissolution (dealloying) of the less active metal Ag, a highly stable nanoporous Au (NPG) framework that can be further functionalized is generated. Also, catalyst activity of the thin film fabricated above was tested toward formic acid oxidation. The results demonstrate that Pt-NPG thin films on Au have higher catalytic activity. The Pt-NPG thin films have lasted over 2600 cycles in standard formic acid oxidation testing, and the peak current densities in the range of 40−50 mA cm^{-2} have been observed resulting in mass activities of 1−3 A mg^{-1} (of combined Pt—Au catalyst).[5] However, the morphology of the NPG thin film deposited on GC exhibited isolated clusters with low nucleation density and a considerable loss was observed following testing. In order to solve these problems, a seeding method has been introduced in order to plant different metal sites on the GC surface to enhance nucleation density and fabricate eventually a continuous

Received: November 28, 2015
Revised: January 5, 2016
Published: January 7, 2016

DOI: 10.1021/acs.jpcc.5b11637
J. Phys. Chem. C 2016, 120, 2299−2308

layer.[6,7] Also, electrochemical oxidation[8] and thermochemical oxidation pretreatment[9] of GC have been studied, compared and found as feasible approaches for enhancing the adhesion between NPG and GC substrate.

To explore alternative avenues for electrochemical fabrication of NPG, this report shifts the focus to $Cu_xAu_{(1-x)}$ bulk and nanoparticle (nanorod) alloys as precursor materials. Cu is a more catalytically active metal in relevant electrocatalytic processes and has lower cost than Ag, which is a primary constituent of the Ag—Au alloys typically used for NPG synthesis.[5,10] In recent decades, Cu—Au alloys have been studied in various directions. The dealloying behavior of Cu_3Au bulk alloys has been reported by Moffat et al.[10] using electrochemistry and scanning tunneling microscopy (STM). Also, a recent work of Kozaderov et al.[11] suggested monotonic dependence of the dealloying critical potential, E_c with composition of Cu—Au alloys ranging from 0.80 to 0.96 Cu atomic fraction. Pickering et al. have demonstrated surface roughening of Cu—Au alloys during electrolytic dissolution,[12,13] and Weissmuller et al. studied the crack mitigation phenomenon during dealloying of $Cu_{0.75}Au_{0.25}$ (Cu_3Au).[14] In addition, Renner et al. primarily focused on the study of the (111) single crystalline Cu_3Au alloy.[15,16] Work has been done by these authors on studying the influence of halides on the initial anodic dissolution of Cu_3Au (111)[17,18] while efforts of other groups focus on the behavior of Cu—Au thin films[19−21] synthesized through free-corrosion approach or DC magnetron sputtering. Even though extensive work has been done on the Cu—Au system, detailed analysis of the structure, composition and size impact on electrochemical dealloying behavior and on the specific structural aspects of the resulting NPG layer has not yet been reported.

The research in this paper primarily focuses on (i) the systematic study of the dealloying of $Cu_xAu_{(1-x)}$ bulk alloys with different composition (x = 0.7 and 0.8), with interest in the dealloying critical potential and resulting dealloyed structures, (ii) investigation of the stability of intermetallic and random alloy nanorods with composition of Cu_3Au and comparison with the dealloying of their bulk counterparts; and (iii) assessment of the catalytic activity toward formic acid oxidation of both types of nanorods coated with an ultrathin Pt films in order to explore the use of nanoporous and nanoparticulate Au-based frameworks as carriers of catalytically active materials for fuel cell applications.

In this work, employing previously developed routines, a study of the dealloying behavior of different composition $Cu_xAu_{(1-x)}$ polycrystalline bulk alloys is carried out, and the structural characteristics of the resulting NPG structures have been discussed. The results are compared with those previously reported in the literature obtained in the same system but at different compositions.[10,22] Along with the dealloying behavior, Pb underpotential deposition (UPD) method is used to examine the change of surface area,[23] scanning electron microscopy (SEM) is employed to image the morphology before and after dealloying, and X-ray diffraction (XRD) is used to analyze the potential presence of multiple phases and/or orientations. Another key component of our objectives in this paper is the study of the dealloying by linear sweep voltammetry and electrochemical quartz-crystal microbalance (EQCM) on Cu_3Au nanorods synthesized using our established routines[24] which employed a seeded growth (Au nanoparticulated seed) followed by a coreduction method. In this work, two types of Cu_3Au nanorods, intermetallic and random alloy, are subjected to dealloying and their behavior and resulting materials are compared to their bulk counterparts. This comparison elucidates the size and structure effects on the dealloying in the Cu—Au system. The original interest in the dealloying of such structures stems from previous reports suggesting that their optical and catalytic properties can be tuned by the composition ratio which might be affected by progressive Cu loss during the course of the specific application.[24−28] Finally, basic tests on catalytic properties of Pt-coated nanorod structures during formic acid oxidation are reported and discussed with focus on shape and structural differences.[5,29]

2. EXPERIMENTAL SECTION

2.1. Electrode Preparation. $Cu_xAu_{(1-x)}$ (x = 0.7 and 0.8) bulk alloy strips (3.0 × 0.5 cm^2) of thickness ca. 250 μm were polished with a cotton applicator using 1 μm alumina slurry (Buehler, Lake Bluff, IL, U.S.A.), then rinsed by Barnstead Nanopure water ($R \geq 18.2$ MΩ cm) and sonicated for 2 min in water. After sonication, the strips were dried under ultra high purity N_2 (less than 1 ppb of O_2, CO, CO_2, and moisture). The size of the dealloying area is 0.5 × 0.5 cm^2, and areas that were to be excluded from dealloying were coated with nail polish.

2.2. Synthesis of Intermetallic and Random Alloy Nanorods. The nanorods were synthesized using our previously reported procedure.[24] Briefly, 20 mmol tetradecylamine (TDA, T.C.I., >95%) and hydrogen tetrachloroaurate trihydrate ($HAuCl_4 \cdot 3H_2O$, Alfa Aeser, 99.9%, 0.05 mmol, 19.7 mg) were added to a 25 mL three-neck flask equipped with a magnetic stir bar. Argon was used to purge the reaction mixture for 10 min to remove O_2. The reaction mixture was heated directly to 160 °C and maintained for 20 min. Without separation, copper 2,4-pentanedionate ($Cu(acac)_2$, Alfa Aeser, 98%, 52.4 mg, 0.2 mmol) in 1 mL of oleylamine (OLA, Sigma-Aldrich, 70%) was then injected to the reaction mixture, followed by heating the reaction mixture directly to 210 °C and maintaining for another 20 min. For synthesis of Cu_3Au intermetallic nanorods, the reaction mixture was further heated to 280 °C and kept at this temperature for another 20 min. After the reaction, the product was purified by adding toluene and centrifuging at 3300 rpm for 2 min to remove excess reactants and surfactants. The nanorod protected by the surfactant amines (i.e., TDA and OLA) were collected and redispersed in oil-based organic solvents such as toluene. These nanorods were transferred from organic to aqueous phase by displacing the surface-bounded aliphatic amines with methoxypolyethylene glycol amine (PEG-NH_2, Alfa Aeser, M.W. = 5000) in a common solvent. Briefly, approximately 2 mg Cu_3Au nanorods were dispersed in 1 mg/mL PEG-NH_2 of chloroform solution and incubated overnight, followed by washing in sequence using hexanes, ethanol, and water. After phase transfer from organic solvent to aqueous solution, the nanorods were suspended in water for future use.

2.3. Drop Casting. Drop casting method was used to coat diluted nanorod suspension on a GC rotation disk electrode. Before dilution, stock solutions of Nafion and nanorods were sonicated to ensure homogeneity. After thorough sonication, the samples were diluted to a final concentration of 1.0 mg/mL with the 0.05% Nafion solution. By using a micropipette, the sample was deposited on electrode (15 μL for a 3 mm GC working electrode) and allowed to dry slowly. This procedure was repeated three times, yielding a loading of 2.25 mg/cm^2 of nanorods.

DOI: 10.1021/acs.jpcc.5b11637
J. Phys. Chem. C 2016, 120, 2299−2308

2.4. Dealloying Process. Selective removal of Cu from the Cu—Au poly alloy (dealloying) was carried out by linear sweep voltammetry to obtain NPG. The dealloying experiments were performed in a three-electrode cell filled with 1 mM $CuSO_4$ and 0.1 M $HClO_4$ (GFS Chemical, 70% redistilled). A Pt wire was used as the counter electrode (CE). A PAR Model 273 Potentiostat/Glavanostat with Corrware Software was used to perform anodic scans from 0.10 to 1.20 V versus Cu/Cu^{2+} pseudo reference electrode (PRE) at sweep rate of 1 mV s^{-1}.

2.5. Surface Area (SA) Measurements: Pb UPD. Pb UPD was performed before and after dealloying each time to determine the SA of as-polished $Cu_xAu_{(1-x)}$ precursor and the synthesized NPG. The measurements were performed by cyclic voltammetry in a three-electrode cell with Pt wire that served as CE. The solution used for Pb UPD contains 0.1 M $NaClO_4$ (Sigma, 99.95%), 3 mM $Pb(ClO_4)_2$ (Aldrich, 99.995%), and 0.01 M $HClO_4$. The solution was purged with ultra high purity N_2 for 20 min prior to Pb UPD experiments, followed by gently passing N_2 over the surface of the solution during the anodic scans. A BASi Epsilon Electrochemical Workstation was used for cycling the potential at 20 mVs^{-1} from 0.600 to 0.010 V versus Pb/Pb^{2+}PRE (−0.200 V vs standard hydrogen electrode, SHE). Functionalized electrodes were assessed for SA by H UPD performed on the surface from +0.400 to −0.680 V at 50 mV s^{-1} vs SSE in a 0.5 M H_2SO_4 (GFS Chemical, redistilled 95−98%) solution following routines for measuring electrochemically active surface area (ECASA).[30] The solution was purged with nitrogen for 2 h prior to H UPD and had N_2 gas passed over the surface of the solution during the analysis. The charge was calculated by integrating the current of the anodic and cathodic scans in the H UPD range, followed by averaging the charges of both curves.[5] In all electrochemical experiments, the masked Cu—Au bulk alloys were immersed in the dealloying solution while the nanorods coated on glassy carbon electrodes were in contact with the electrolyte in hanging meniscus configuration as described elsewhere.[31]

2.6. X-ray Diffraction, SEM, TEM, and Compositional Analysis. XRD results were obtained on a Scintag XDS2000, θ-2θ configuration powder diffractometer equipped with a Ge-(Li) solid-state detector (Cu KR radiation). Unmasked portion of as-polished bulk alloys was analyzed to determine specific phases and orientations. Scanning Electron Microscopy (SEM, Zeiss Supra 55 VP) coupled with an in-lens detector at an accelerating voltage of 10 kV and a working distance of 2 mm was performed for morphological characterization of dealloyed bulk alloy strips. Also, the same instrument coupled with an EDS detector (EDAX) at accelerating voltage of 10 kV and working distance of 8.5 mm was used for the compositional analysis of as-polished $Cu_xAu_{(1-x)}$ bulk alloy samples (for confirming the initial composition) and $Cu_{0.8}Au_{0.2}$ dealloyed with total anodic charge of 20 $C.cm^{-2}$ at potentials of 0.68 and 0.88 V versus Cu/Cu^{2+} PRE (for assessing the extent of potential Cu retention in both cases). Transmission electron microscopy (TEM) was carried out to characterize the size and shape of NPs. TEM imaging was performed at an acceleration voltage of 100 kV using a JEOL cx100.

2.7. EQCM Measurements. EQCM measurements were performed with a model QCM200 Quartz Crystal Microbalance Digital Controller (Stanford Research Systems). The crystal used has a resonant frequency of f_o = 5.000 MHz, density of ρ = 2.648 g cm^{-3}, and shear modulus of $\mu = 2.947 \times 10^{11}$ g cm^{-1} s^{-2}. Analysis of the Sauerbrey eq (eq 1)[32] indicates that a 0.1 Hz frequency change corresponds to a mass change of 0.18 ng.[33]

$$\Delta f = \frac{-2f_0^{\,2}}{A\sqrt{\mu\rho}}\Delta m \tag{1}$$

2.8. Functionalization with Pt. Five replacements of a Pb UPD layer by Pt(II)Cl complex[5,34] were carried out using surface-limited redox replacement with an OMNI 90 (Cypress Systems) potentiostat coupled to a National Instruments analog-to-digital converting board. The platinization was performed in a solution containing 0.1 M $NaClO_4$ (Sigma, 99.95%), 1 mM $HClO_4$, 1 mM $Pb(ClO_4)_2$, and 0.5 mM $KPtCl_4$ (GFS Chemical, 98%) and recorded using Dasylab 9.00 software, following a protocol recently developed by our group.[5,34] A 1 s pulse at −0.830 V vs mercury-mercurous sulfate, MSE was applied to allow percolation of the Pb throughout the nanoporous structure. Then applied potential was released and the potential was monitored until it reached +0.050 V. At this high limit, the pulse was reapplied and the cycle resumed for each replacement.

2.9. Formic Acid Oxidation. Prior to formic acid oxidation, the samples were electrochemically annealed by rapidly scanning (300 mV s^{-1}) between −0.740 and +0.450 V in the H UPD solution for 50 cycles to activate the surface. The testing followed a procedure developed and described in our earlier work.[35] More specifically, formic acid oxidation was performed on the Pt-NPG surface in 2 M HCOOH (JT Baker, 88%), and 0.1 M $HClO_4$ from −0.510 to +0.800 V vs MSE repetitively until the current density decayed to about zero. After a certain number of cycles, the working electrode was removed from the formic acid cell and checked with H UPD to assess the surface quality and to measure ECASA.[30]

3. RESULTS AND DISCUSSION

3.1. Dealloying Properties of Bulk Alloy. The dealloying behavior of $Cu_{0.8}Au_{0.2}$ and $Cu_{0.7}Au_{0.3}$ strips was carried out. Figure 1 presents the potentiodynamic polarization behavior of both bulk alloys strips. At the beginning of dealloying, a small peak appears at about 0.2 V vs Cu/Cu^{2+} PRE for both samples, labeled as stage I in this work. Similar peaks are also seen in work by Moffat et al.,[10] and its appearance is attributed to oxidation of Cu from nonbonded or low coordination surface sites.[15] This is potentially associated with the presence of a small portion of Cu-rich solid solution beyond the intended *fcc one*. After stage I, the current exhibits a slow increase at 0.54 and 0.75 V for $Cu_{0.8}Au_{0.2}$ and $Cu_{0.7}Au_{0.3}$, respectively. This marks the onset of stage II as labeled in Figure 1. Stage III begins with a sharp current increase occurring at 0.8 and 1.0 V for $Cu_{0.8}Au_{0.2}$ and $Cu_{0.7}Au_{0.3}$, respectively. This observation suggests multistage dealloying in the Cu—Au system that is quite different than the characteristic Ag—Au dealloying layout.[29] More specifically, the Ag—Au system features no dissolution of weakly bonded Ag, and its dealloying polarization curve contains only one sharp current increase associated with the onset of Ag dissolution positive to the critical potential, E_c. The lack of different dealloying regimes in the Ag—Au system is likely associated with the virtually ideal miscibility between Ag and Au over the entire compositional range as well as with the absence of thermodynamically stable intermetallic compounds. Further details of the comparison between Ag—Au and Cu—Au systems can be found in the work of Wei et al.[36] where the analysis of both phase diagrams is provided.

DOI: 10.1021/acs.jpcc.5b11637
J. Phys. Chem. C 2016, 120, 2299−2308

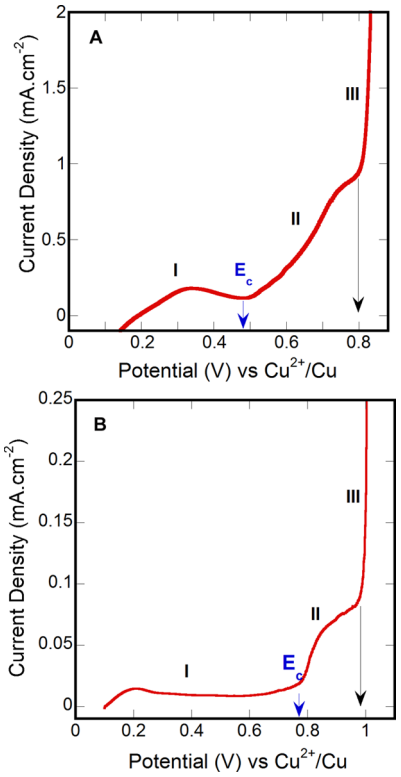

Figure 1. Anodic polarization curves for (A) $Cu_{0.8}Au_{0.2}$ and (B) $Cu_{0.7}Au_{0.3}$ polycrystalline bulk alloys strips at a sweep rate of 1 mV s^{-1}.

The complexity of the anodic polarization curves of samples with different composition (Figure 1) makes ambiguous the visual determination of the E_c in the studied system herein. Running into the same difficulty of determining the E_c, Moffat et al.,[10] performed current decay measurements at different potentials. This chronoamperometry based approach, claimed later by Corcoran et al. to be the most accurate method for determining the dealloying critical potential[37] relies on discrimination between decaying and nondecaying current upon polarization at different potentials to pinpoint the accurate E_c value. In ref 10, 0.25 V vs SSE as the E_c for Cu_3Au bulk alloy was determined using this approach. Also, E_c for the dealloying of Cu—Au alloys with Cu atomic fraction in the range 0.80 to 0.96 has been determined using the chronoamperometry approach in Cu^{2+} solution with pH 3.3[11] and the results recalculated vs Cu^{2+}/Cu PRE are presented for comparison in Table 1. In order to fully understand the Cu dissolution behavior, determine the critical potential, and compare our results with those presented in literature, the chronoamperometry method has also been used in this work, and the obtained curves are presented in Figure 2. For

Table 1. Critical Potential (E_c) Comparison for the Dealloying of Bulk $Cu_xAu_{(1-x)}$ Alloy in the Range of x from 0.70 to 0.96

sample	E_c vs Cu^{2+}/Cu PRE
$Cu_{96}Au_4$ [from ref 11]	0.08 V
$Cu_{90}Au_{10}$ [from ref 11]	0.11 V
$Cu_{85}Au_{15}$ [from ref 11]	0.34 V
$Cu_{80}Au_{20}$ [from ref 11]	0.52 V
$Cu_{80}Au_{20}$	0.54 V
$Cu_{75}Au_{25}$(Cu_3Au) [from ref 10]	0.65 V
$Cu_{70}Au_{30}$	0.72 V

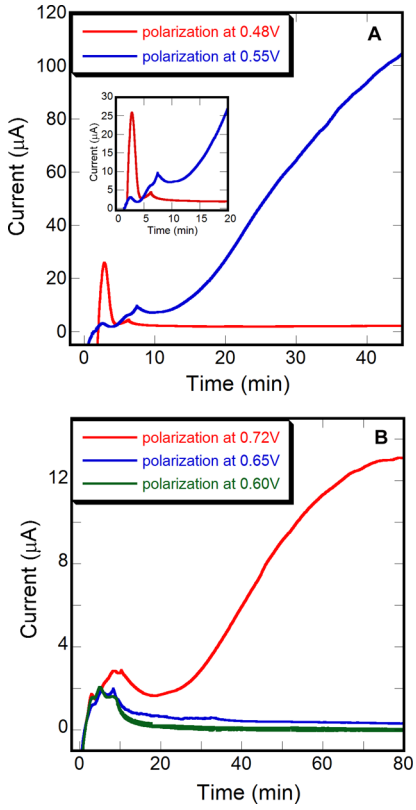

Figure 2. Current decays registered during dealloying of (A) $Cu_{0.8}Au_{0.2}$ and (B) $Cu_{0.7}Au_{0.3}$ polycrystalline bulk alloys at various potentials. Inset: Magnified plot (A) for better illustration.

$Cu_{0.8}Au_{0.2}$ alloys, the current generally decays slowly negative of 0.54 V (Figure 2A, inset). When the potential is higher than 0.54 V, the current increases initially and eventually levels off after long time of dealloying (not shown). A similar phenomenon was seen for the $Cu_{0.7}Au_{0.3}$ samples, suggesting alike with Figure 2A a decaying current only in the potential range negative of 0.72 V and a current that increases to saturation at more positive potentials. These results clearly place the E_c for $Cu_{0.8}Au_{0.2}$ and $Cu_{0.7}Au_{0.3}$ at 0.54 and 0.72 V vs Cu/Cu^{2+} PRE, respectively, thus demonstrating that the onset of stage II is the actual beginning of bulk Cu dealloying. In light of this finding, the results by Moffat et al.[10] and Kozaderov et al.[11] suggest identical behavior of alloys with different composition and confirm the beginning of stage II as the onset of bulk dealloying in the Cu—Au system.

Table 1 presents the comparison of critical potentials for $Cu_xAu_{(1-x)}$ bulk alloys studied in our work and in references.[10,11] As seen in Table 1, the clear monotonic trend in E_c shows undoubtedly E_c dependence upon the alloy composition. Here, the slight difference of 0.02 V in the critical potentials in $Cu_{0.80}Au_{0.20}$ could be likely attributed to differences in pH and Cu^{2+} ion concentration. Overall, similarly to what is observed in Au—Ag alloys[38] the critical potential shifts positively with the increase of the Au content in the alloy. Such behavior was also observed, by Yang et al.[39] for the dealloying of Cu—Pt alloys. This characteristic dependence for many binary alloy systems associates the increase of the more noble metal content with the increase of the average number of

DOI: 10.1021/acs.jpcc.5b11637
J. Phys. Chem. C 2016, 120, 2299−2308

coordinating Au atoms around each Cu atom (decrease of the average Cu cluster size) that in turn raises the barrier of Cu dissolution from Cu—Au alloys.

At this point, the reason and principle of the existence of two regimes of bulk dealloying (stages II and III) is still unknown. In order to understand this current density increase, two identical $Cu_{0.8}Au_{0.2}$ samples were selected for comparison. One sample was dealloyed at a potential of 0.68 V vs Cu/Cu^{2+} PRE, (into stage II); another sample was dealloyed at a potential of 0.88 V into stage III. Both samples were dealloyed at identical conditions until a total anodic charge of 1200 $mC{\cdot}cm^{-2}$ was accumulated to ensure the removal of identical amount of Cu. Pb UPD has also been used to determine the surface area evolution before and after dealloying.[23] Figure 3 presents the

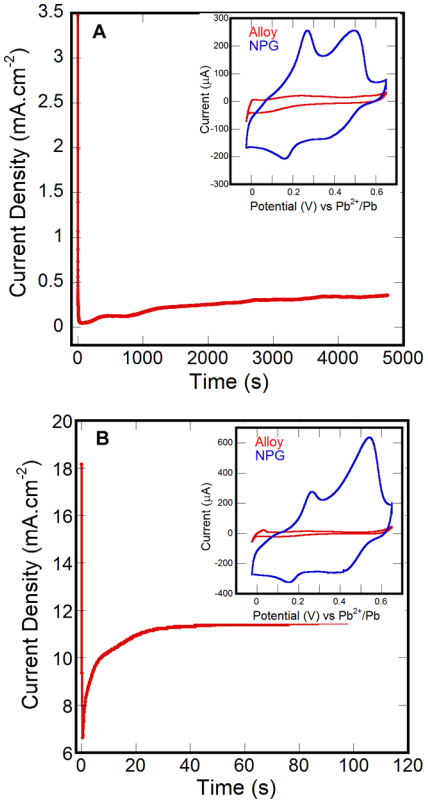

Figure 3. Chronoamperometry curves of $Cu_{0.8}Au_{0.2}$ alloy at (A) higher (0.68 V) and (B) lower (0.88 V) potential. Insets: Pb UPD curves before and after dealloying at above-mentioned potentials. Sweep rate: 20 $mV.s^{-1}$.

dealloying curve at lower (0.68 V, stage II) and higher (0.88 V, stage III) potential with their Pb UPD SA characterization results inserted, and Table 2 demonstrates the Pb UPD assay results associated with SA development after the dealloying process. The results illustrate that the SA of the stage III sample is ca. 85 times higher than the flat Au surface. Comparing the roughness factor (Rf) from our pervious paper,[23] the SA development at the same dealloying depth for $Ag_{0.8}Au_{0.2}$ is around 75 times higher than that of a flat Au surface, indicating that equivalent or higher SA increase can be generated in $Cu_xAu_{(1-x)}$ alloy system under identical dealloying conditions. In addition, Cu is generally a better catalyst and has lower cost in comparison with Ag, therefore, fabricating NPG using $Cu_xAu_{(1-x)}$ alloys would be more effective and economical.

Table 2. Pb UPD Assessment of Surface Development after De-alloying of $Cu_{0.8}Au_{0.2}$ Alloy at Lower and Higher Potential

sample	charge stripped (mC/cm^2)	SA of Cu—Au strip (cm^2)	SA after dealloying (cm^2)	SA development
de-alloyed at 0.68 V	1200	0.25	12.96	51.83
de-alloyed at 0.88 V	1200	0.25	21.13	84.52

From the dealloying curves it can also be observed that when the bulk alloy was dealloyed at 0.68 V, the current density was 0.25 $mA{\cdot}cm^{-2}$, while the current density at dealloying voltage of 0.88 V was more than 40 times higher with the average number of 11 $mA{\cdot}cm^{-2}$. Therefore, the dissolution of identical amounts of Cu took substantially shorter time at the higher dealloying potential, which has been quantitatively determined by chronocoulometry. Comparing the behavior of Pb UPD in Figure 3 and Table 2, the SA development after dealloying at 0.88 V is about twice as high as that obtained after dealloying at 0.68 V. Moreover, after completion of the dealloying process, SEM was used to characterize the morphology of the samples as shown in Figure 4. In support of the SA characterization

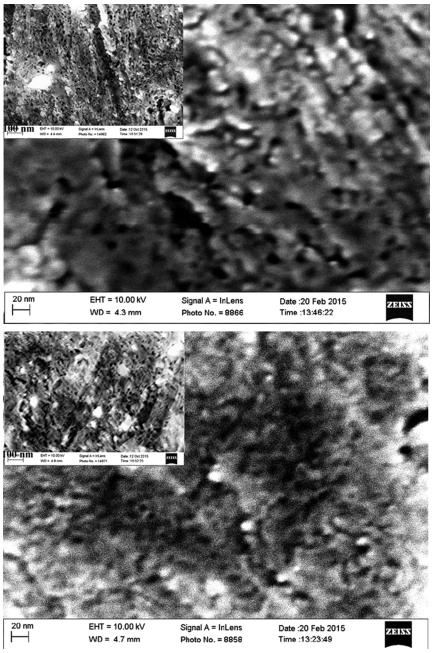

Figure 4. SEM images after dealloying of $Cu_{0.8}Au_{0.2}$ alloy at (A) lower (0.68 V) and (B) higher (0.88 V) potentials. Insets: Lower resolution SEM images, respectively.

results, larger but more isolated holes were observed in 0.68 V sample while the holes in 0.88 V sample appeared smaller and more homogeneously distributed on the surface. Overall, the latter case results in the formation of a structure with about 0.5 pore fraction while in the former case, the pores seem to occupy no more than a third of the surface. The difference in both morphologies could be a result of different rates of Cu retention upon dealloying.[40] Indeed, the dramatic difference in dealloying current density in both cases could lead to more complete Cu dissolution at 0.88 V where the process is faster and the restructuring Au has less time to passivate large enough surface area. EDS experiments carried out on deeply dealloyed

DOI: 10.1021/acs.jpcc.5b11637
J. Phys. Chem. C 2016, 120, 2299−2308

in stage II and stage III $Cu_{0.8}Au_{0.2}$ alloys (total anodic charge of 20.0 $C{\cdot}cm^{-2}$) suggested Cu retention of 35% versus 25%, respectively, which confirmed the above analysis. Similar results suggesting potential dependence of the rate of less-noble metal retention were obtained on dealloyed $Ag_{0.8}Au_{0.2}$ in earlier work of our group.[40]

The systematic study of bulk $Cu_xAu_{(1-x)}$ dealloying also revealed slight differences in the anodic polarization curves of same-composition alloys. The differences mainly manifest themselves in the magnitudes of current increase in stage II and to a small extent in the starting point of stage III. To look deeper into these differences, an XRD characterization was performed. In Figure 5, the XRD patterns of three $Cu_{0.8}Au_{0.2}$ bulk alloy samples originating from a common source sheet are presented with their respective dealloying curves inserted. The source alloy sheet was made by melting a mix of single components followed by quenching and subsequent rolling. Compared with the Cu_3Au XRD pattern studied elsewhere,[19] different orientations are labeled in Figure 5. A coexistence of various orientations in the bulk alloys has been observed at different ratios. This reveals the presence of grains with different size and orientation in the otherwise homogeneous $Cu_{0.8}Au_{0.2}$ alloy. It is noteworthy that the dealloying kinetics in stage II seem to differ substantially with the Cu dissolution process in that potential range being least active on alloys with substantial presence of a (311) face known to consist of (100) terraces and (111) steps for *fcc* metals.[41] Also, earlier XRD work on Cu_3Au alloy structure associates the (311) face with larger terraces, higher steps and the best mixing between Cu and Au on all (100) terraces.[42] This could then support the speculation that stage II is prompted by the dissolution of Cu from terraces with orientation other than (100) and/or from defects and irregularities statistically adequate to the specific alloy composition. Apparently, further work and more comprehensive analysis that go beyond the scope of this work need to be done to verify this speculation.

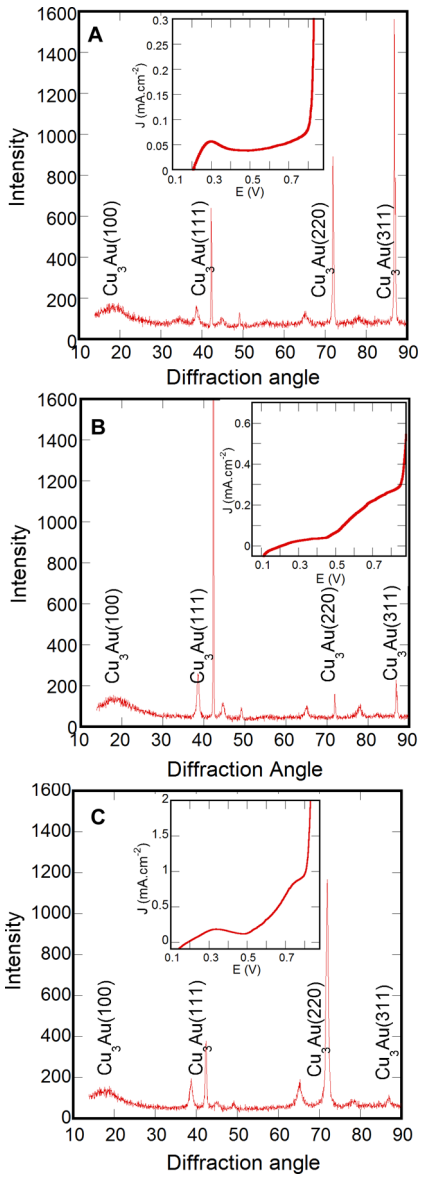

Figure 5. XRD patterns of three identical $Cu_{0.8}Au_{0.2}$ bulk alloy samples. Insets: Dealloying (anodic polarization) curves at a sweep rate of 1 $mV{\cdot}s^{-1}$ for these samples, respectively.

3.2. Dealloying Properties of Cu_3Au Nanorods. Two types of Cu_3Au nanorods, (A) intermetallic and (B) random alloy, were studied. The TEM images before and after phase transfer of the nanorods from organic solvent toluene to aqueous solution are shown in Figure 6. Before the phase transfer, the average size of the intermetallic nanorods is 19 ± 3 nm at length and 10 ± 1 nm at width while the average size of the alloyed nanorods is 23 ± 4 nm at length and 9 ± 1 nm at width. There is little difference in size for both samples after the phase transfer.

Figure 7 shows the dealloying curves of sample A and B, and the inset is the magnified range between 0.3 and 0.8 V vs the Cu/Cu^{2+} PRE. On the basis of Figure 7, both samples (intermetallic, A and random alloy, B) exhibit very clear dealloying behavior with the Cu selective dissolution parting taking off at 0.4 V positive vs the Cu/Cu^{2+} reversible potential. Other than that, comparing the dealloying behavior between sample A and B, small differences associated with slightly negative (at most 0.020−0.025 V) dealloying onset for sample B and also slightly faster dealloying kinetics for sample B have been seen by the anodic polarization curves comparison. An estimate of the E_c difference between samples A and B could be made by considering the difference in enthalpy of mixing, ΔH_{mix}, between the solid solution and the intermetallic compound found to be in the range 3 to 4 kJ mol^{-1}.[43] Next, assuming no significant difference in the entropy of mixing in both cases that leads to $\Delta H_{mix} \approx \Delta G_{mix}$ (ΔG_{mix} is the Gibbs Free Energy of mixing), one obtains a potential shift $E = \Delta G_{mix}/zF$ (z is the oxidation number of Cu, and F is the Faraday constant) in the range of 0.015 to 0.020 V. This estimate is in good agreement with the experimental result and as such supports the conclusion that the random alloy (B) could be considered as just slightly more reactive and thereby less stable in comparison with the intermetallic compound (A).

To further confirm the apparent dealloying critical potential of nanoscale Cu_3Au alloys, EQCM was used. Figure 8 shows a potential/frequency curve (the blue line) aligned with the respective dealloying curve (the red line) both registered simultaneously for the intermetallic sample, A. The analysis of both curves suggests that the onset of the anodic current increase with onset around 0.40 V vs Cu/Cu^{2+} is associated with changes of mass in the sample. More specifically, in this plot the frequency increase relates directly to a mass decrease. This clearly indicates that positive to 0.40 V, the more reactive metal (Cu) starts to dissolve. The frequency keeps increasing

DOI: 10.1021/acs.jpcc.5b11637
J. Phys. Chem. C 2016, 120, 2299−2308

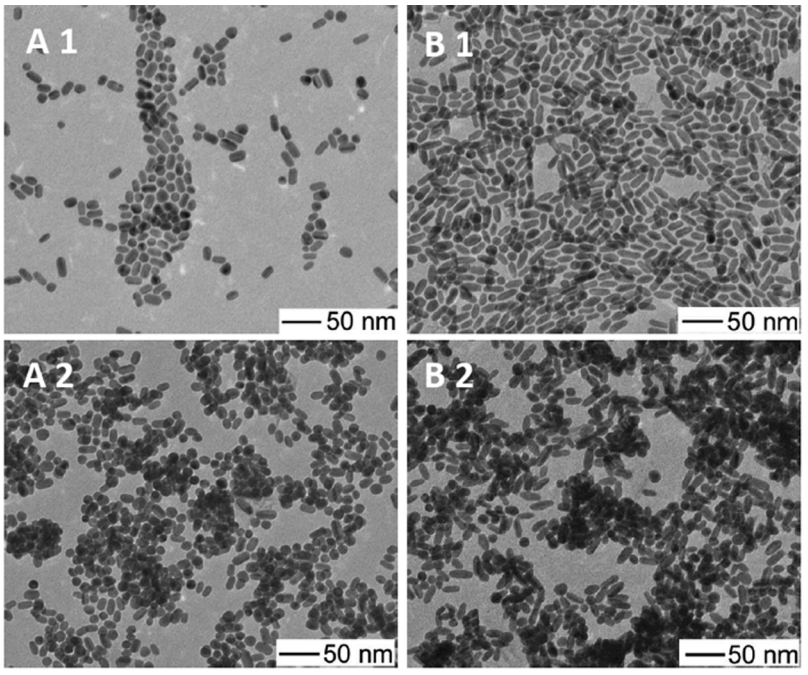

Figure 6. TEM images of as-synthesized Cu_3Au nanorods before and after phase transfer of the nanorods from organic solvent toluene to aqueous solution: (A1) intermetallic, (B1) alloy. (A2) intermetallic post phase transfer, (B2) alloy post phase transfer.

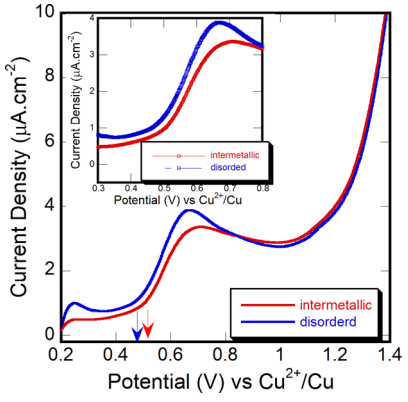

Figure 7. Anodic polarization curves for Cu_3Au nanorods at a sweep rate of 1 $mV{\cdot}s^{-1}$. Insets: Narrow potential ranges for the dealloying of both alloys, respectively.

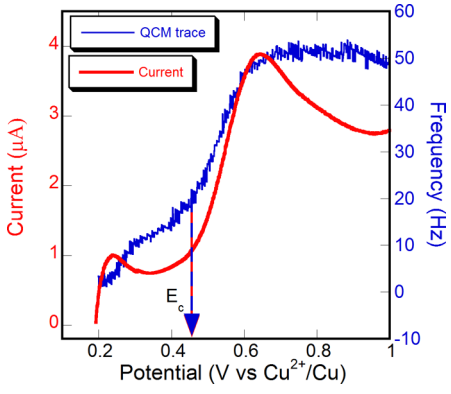

Figure 8. Anodic polarization curve (sweep rate 1 $mV{\cdot}s^{-1}$), blue and QC frequency curve, red simultaneously obtained for intermetallic nanorods.

and when the potential reaches 0.60 V vs Cu/Cu^{2+} reversible potential, the frequency stops increasing and levels off around 50 Hz. Combining these two lines, a conclusion can be drawn that the dealloying process is over at around 0.60 V owing to a complete Cu dissolution. After that point, the mass remains stable, and the frequency remains constant as well. Overall, the QCM curve confirmed that the critical potential is at about 0.38−0.40 V for intermetallic nanorods and dealloying ceases around 0.60 V. As mentioned above, according to ref 10, the dealloying critical potential for Cu_3Au bulk alloy is at 0.65 V vs Cu/Cu^{2+} reversible potential. The apparent difference of about 0.25 V between the bulk phase and nanophase alloys clearly confirms the trend reported in our previous work where a comprehensive comparison involving multiple compositions of bulk and nano Ag—Au alloys showed negative shifts of as high as 0.40 V in comparison with alloyed nanoparticles of identical composition.[29] As mentioned earlier,[29] this magnitude of a negative shift associated with Gibbs−Thomson (curvature) effect exceeds substantially the values (order of 0.05 V) predicted theoretically[44] and measured experimentally for pure Ag and Au nanoparticles.[45] Such discrepancy is still unexplained owing to the absence of adequate mathematical model that would take into account all factors governing the nanophase dealloying. Yet, it appears that owing to specific microstructural effects the higher curvature lowers the stability of single phase alloys (Ag—Au and Cu—Au) substantially more than the same effects impact stability of pure metal constituents of the respective alloys.

3.3. Formic Acid Testing of Cu—Au Nanorods. In this work, as-synthesized and dealloyed intermetallic nanorods (sample A) were platinized and then tested for formic acid activity. The platinization was administered by coating of both nanorods with several monolayers of Pt using SLRR of Pb UPD layer by Pt (II) complex.[5,34] Five replacements of Pb by Pt were performed to generate a Pt thin film. The potential transients for these replacements are shown in the inset of Figure 9. After

DOI: 10.1021/acs.jpcc.5b11637
J. Phys. Chem. C 2016, 120, 2299−2308

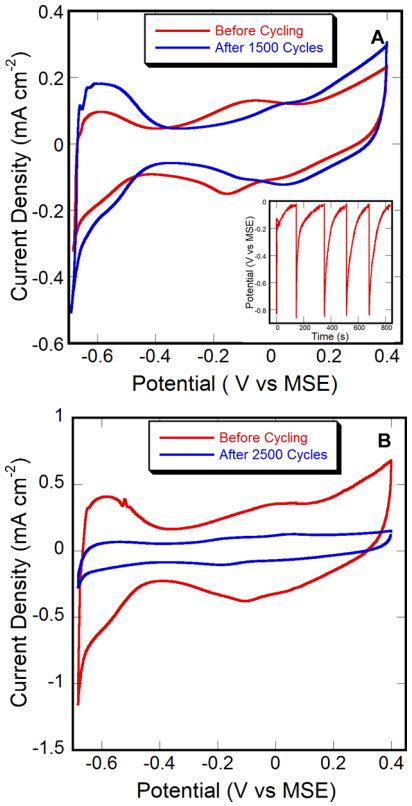

Figure 9. CV curves (sweep rate: 50 mV·s^{-1}) showing H UPD results on platinized (A) as-synthesized nanorods and (B) dealloyed Cu_3Au nanorods. Inset: Chronopotentiometry curve showing the potential behavior of Cu_3Au nanorods during 5 SLRR platinization cycles.

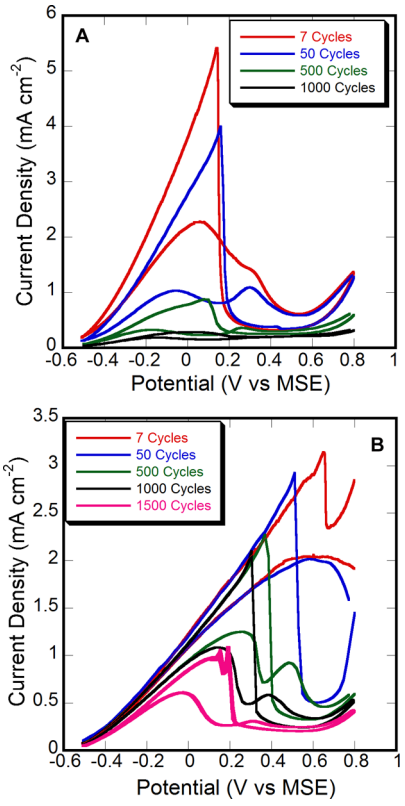

Figure 10. CV curves for formic acid oxidation on platinized (A) as-synthesized nanorods and (B) dealloyed Cu_3Au nanorods. Sweep rate: 50 mV·s^{-1}.

the Pt coating was completed, H UPD was used to perform ECASA measurements on the coated surface. Figure 9 shows detailed characteristic peaks of H UPD formation and stripping on/from the platinized surface in the −0.670 to 0.400 V potential range.

The CV curves presented in Figure 10 illustrate the formic acid oxidation behavior of Pt-coated intermetallic nanorods after different number of cycles. A comparison of the anodic scans of both (red) CV curves after 7 cycles suggests that CO adsorption on the electrode begins at approximately 0.45 V for dealloyed intermetallic nanorods and 0.30 V for Cu_3Au nanorods. The catalysts activity in these tests was measured on negative potential scanning when the passivity layer was broken and a fresh surface revealed, a current peak was recorded. It is noteworthy that the substantial oxidation current density increase occurs at about 0.400 V for dealloyed and at 0.200 V for nondealloyed nanorods. This difference implies better oxidation and CO poisoning tolerance of the dealloyed intermetallic nanorods. Also, the formic acid oxidation showed high activity initially for the catalysts on both nanorods, with peak current densities of about 3.5 to 5.5 mA·cm^{-2}, respectively. These values are well in the realm of Pt or Pt-based alloy nanoparticles shown previously to produce peak current densities of about 2.5 mA·cm^{-2} and 4.0 mA·cm^{-2}, respectively.[35,46] On the basis of these current densities, peak mass activity values developed in this work account for c.a. 0.5 A·mg^{-1} of combined Pt—Au—Cu content. The results of the formic acid oxidation testing overall illustrate that catalysts generated as-synthesized and dealloyed Cu_3Au nanorods have comparable activity performance to those of same-size Pt or Pt-based alloy nanoparticulate catalysts. In addition, comparing the nanorods before and after dealloying, the catalysts developed on dealloyed nanorods exhibit qualitatively different behavior manifested by virtually lacking hysteresis in the very beginning followed by a negatively shifting peak with cycling in the cathodic sweep. This behavior compared to the typical distinct hysteresis in CV curve and constant peak potential in the cathodic scan seen in the testing of as-synthesized catalyst implies higher applicability to the formic acid oxidation of the dealloyed catalyst. The latter conclusion is further supported by the better durability performance of the dealloyed catalyst lasting for well over 1500 cycles. This difference between both catalysts may be due to retention of some Cu during the dealloying of nanorods and in turn to the formation of Cu-core and Au shell particles that would accommodate the coating Pt differently than the pure Au or Cu_3Au nanoparticles.[47] The impact of such effects on the catalytic activity however will be studied in detail in future work. Overall, Pt coating on as-synthesized and dealloyed Cu_3Au nanorods makes catalysts that exhibit high activity and good durability. Therefore, nanoscale Au and nanosized Au-rich frameworks obtained by controlled dealloying of the $Cu_xAu_{(1-x)}$ system can be used as a reliable source of catalytically active materials in different applications.

4. CONCLUSIONS

Unlike Ag—Au alloys, the Cu—Au bulk alloys feature quite different dealloying behavior that manifests itself in the presence of three different stages in the respective anodic polarization curves. On the basis of current decay tests, the onset of stage II is associated with the critical potential for $Cu_{0.8}Au_{0.2}$ and $Cu_{0.7}Au_{0.3}$ bulk alloys, and measured to be 0.54

DOI: 10.1021/acs.jpcc.5b11637
J. Phys. Chem. C 2016, 120, 2299−2308

and 0.72 V, respectively. Beside, the findings of dealloying at lower (in stage II) and higher potential (in stage III) reported in the present work, Pb UPD results and SEM images have shown the difference of these stages, identifying them as ranges of limited and complete dealloying, respectively. XRD results associated with specificity of the dealloying in stage II of $Cu_{0.8}Au_{0.2}$ alloys imply certain dependence of the dealloying kinetics there upon the presence (or absence) of grains with (311) crystallographic orientation. Also, the comprehensive comparison of the dealloying behavior of bulk alloys with different compositions along with results of others suggests conventional potential dependence with the Au content increase of the dealloying critical potential as well as stages II and III of the polarization curves. At the same time, anodic polarization curves along with EQCM tests on two kinds of Cu_3Au nanorods, helped determine the dealloying process taking off at about 0.40−0.43 V positive to the Cu/Cu^{2+} reversible potential for both, with a tiny difference shown between intermetallics and random alloy nanorods. However, the E_c of both types of nanorods has been found to shift negatively (by c.a. of 0.20 V) in comparison with the E_c of their bulk counterpart Cu_3Au alloy.

The results of formic acid oxidation testing have shown good activity and durability performance of Pt-coated Cu_3Au nanorods and the Au enriched structures resulting from their dealloying, which indicate that overall the Cu_3Au nanorods can be good candidates as catalysts supports in fuel cell applications. Due to the high surface-area-to-volume ratio and the good mechanical stability, such materials can serve as base for more effective and low-cost catalysts.

AUTHOR INFORMATION

Corresponding Author

*Phone: +1 (607) 777-4271; fax: +1 (607) 777-4478; e-mail: dimitrov@binghamton.edu (N.D.).

Notes

The authors declare no competing financial interest.

ACKNOWLEDGMENTS

N.D., J.X., and S.A., acknowledge the financial support by the National Science Foundation, Division of Chemistry, CHE-1310297. J.C. and C.C. acknowledge the financial support by the National Science Foundation, EPSCoR Research Infrastructure Improvement Program, IIA-1457888.

REFERENCES

(1) Erlebacher, J.; Aziz, M. J.; Karma, A.; Dimitrov, N.; Sieradzki, K. Evolution of Nanoporosity in Dealloying. *Nature* **2001**, *410*, 450−453.

(2) Wittstock, A.; Biener, J.; Erlebacher, J.; Bäumer, M. *Nanoporous Gold: From an Ancient Technology to a High-Tech Material.*; Royal Society of Chemistry: London, 2012; pp 1−252.

(3) Ding, Y.; Chen, M. W.; Erlebacher, J. Metallic Mesoporous Nanocomposites for Electrocatalysis. *J. Am. Chem. Soc.* **2004**, *126*, 6876−6877.

(4) Ottakam Thotiyl, M. M.; Freunberger, S. A.; Peng, Z. Q.; Chen, Y. H.; Liu, Z.; Bruce, P. G. A Stable Cathode for the Aprotic Li-O-2 Battery. *Nat. Mater.* **2013**, *12*, 1050−1056.

(5) McCurry, D. A.; Kamundi, M.; Fayette, M.; Wafula, F.; Dimitrov, N. All Electrochemical Fabrication of a Platinized Nanoporous Au Thin-Film Catalyst. *ACS Appl. Mater. Interfaces* **2011**, *3*, 4459−4468.

(6) Bromberg, L.; Xia, J.; Fayette, M.; Dimitrov, N. Synthesis of Ultrathin and Continuous Layers of Nanoporous Au on Glassy Carbon Substrate. *J. Electrochem. Soc.* **2014**, *161*, D3001−D3010.

(7) Kamundi, M.; Bromberg, L.; Ogutu, P.; Dimitrov, N. Seeding Strategies for the Deposition of High Density Network of Nanoporous Au Cluster Catalyst on Glassy Carbon Electrodes. *J. Appl. Electrochem.* **2013**, *43*, 879−890.

(8) Xia, J.; Rooney, R.; Ambrozik, S.; Bromberg, L.; Dimitrov, N. Enhanced Adhesion of Ultrathin Nanoporous Au Deposits by Electrochemical Oxidation of Glassy Carbon. *J. Electrochem. Soc.* **2015**, *162*, H308−H316.

(9) Bromberg, L.; Xia, J.; Rooney, R.; Dimitrov, N. Enhanced Adhesion of Continuous Nanoporous Au Layers by Thermochemical Oxidation of Glassy Carbon. *Coatings* **2014**, *4*, 416−432.

(10) Moffat, T.; Fan, F.-R.; Bard, A. Electrochemical and Scanning Tunneling Microscopic Study of Dealloying of Cu_3Au. *J. Electrochem. Soc.* **1991**, *138*, 3224−3235.

(11) Kozaderov, O. A.; Saratova, A. V.; Vvedenskii, A. V. Kinetics of Phase Transformations in the Surface Layer of a Binary Alloy at the Selective Dissolution: Iii. Cu-Au | Cu^{2+} System. *Prot. Met. Phys. Chem. Surf.* **2009**, *45*, 661−668.

(12) Pickering, H. W.; Byrne, P. J. On Preferential Anodic Dissolution of Alloys in the Low-Current Region and the Nature of the Critical Potential. *J. Electrochem. Soc.* **1971**, *118*, 209−215.

(13) Pickering, H. W. The Surface Roughening of a Cu-Au Alloy During Electrolytic Dissolution. *J. Electrochem. Soc.* **1968**, *115*, 690−694.

(14) Zhong, Y.; Markmann, J.; Jin, H.-J.; Ivanisenko, Y.; Kurmanaeva, L.; Weissmuller, J. Crack Mitigation During Dealloying of $Au_{25}Cu_{75}$. *Adv. Eng. Mater.* **2013**, *211*, 1−10.

(15) Pareek, A.; Ankah, G. N.; Cherevko, S.; Ebbinghaus, P.; Mayrhofer, K. J.; Erbe, A.; Renner, F. U. Effect of Thiol Self-Assembled Monolayers and Plasma Polymer Films on Dealloying of Cu−Au Alloys. *RSC Adv.* **2013**, *2013*, 6586−6595.

(16) Pareek, A.; Borodin, S.; Bashir, A.; Ankah, G. N.; Keil, P.; Eckstein, G. A.; Rohwerder, M.; Stratmann, M.; Grunder, Y.; Renner, F. U. Initiation and Inhibition of Dealloying of Single Crystalline $Cu_3au(111)$ Surfaces. *J. Am. Chem. Soc.* **2011**, *133*, 18264−18271.

(17) Renner, F. U.; Stierle, A.; Dosch, H.; Kolb, D. M.; Zegenhagen, J. The Influence of Chloride on the Initial Anodic Dissolution of $Cu_3au(111)$. *Electrochem. Commun.* **2007**, *9*, 1639−1642.

(18) Ankah, G. N.; Pareek, A.; Cherevko, S.; Topalov, A.; Rohwerder, M.; Renner, F. U. The Influence of Halides on the Initial Selective Dissolution of Cu_3Au (111). *Electrochim. Acta* **2012**, *85*, 384−392.

(19) Tynkova, A.; Katona, G. L.; Langer, G. A.; Sidorenko, S. I.; Voloshko, S. M.; Beke, D. L. Formation of Cu_xau_{1-X} Phases by Cold Homogenization of Au/Cu Nanocrystalline Thin Films. *Beilstein J. Nanotechnol.* **2014**, *5*, 1491−1500.

(20) Morrish, R.; Dorame, K.; Muscat, A. J. Formation of Nanoporous Au by Dealloying Aucu Thin Films in Hno_3. *Scr. Mater.* **2011**, *64*, 856−859.

(21) El Mel, A. A.; Boukli-Hacene, F.; Molina-Luna, L.; Bouts, N.; Chauvin, A.; Thiry, D.; Gautron, E.; Gautier, E.; Tessier, P.-Y. Unusual Dealloying Effect in Gold/Copper Alloy Thin Films: The Role of Defects and Column Boundaries in the Formation of Nanoporous Gold. *ACS Appl. Mater. Interfaces* **2015**, *7*, 2310−2321.

(22) Ateya, B. G.; Fritz, J. D.; Pickering, H. W. Kinetics of Dealloying of a Copper-5 Atomic Percent Gold Alloy. *J. Electrochem. Soc.* **1997**, *144*, 2606−2613.

(23) Liu, Y.; Bliznakov, S.; Dimitrov, N. Comprehensive Study of the Application of a Pb Underpotential Deposition-Assisted Method for Surface Area Measurement of Metallic Nanoporous Materials. *J. Phys. Chem. C* **2009**, *113*, 12362−12372.

(24) Chen, S.; Jenkins, S.; Tao, J.; Zhu, Y.; Chen, J. Anisotropic Seeded Growth of Cu-M (M = Au, Pt, or Pd) Bimetallic Nanorods with Tunable Optical and Catalytic Properties. *J. Phys. Chem. C* **2013**, *117*, 8924−8932.

(25) Jenkins, S. V.; Chen, S.; Chen, J. Gold-Copper Alloyed Nanorods for Metal-Catalyzed Organic Reactions: Implication of Surface Ligands on Nanoparticle-Based Heterogeneous Catalysis. *Tetrahedron Lett.* **2015**, *56*, 3368−3372.

DOI: 10.1021/acs.jpcc.5b11637
J. Phys. Chem. C 2016, 120, 2299−2308

(26) Kim, D.; Resasco, J.; Yu, Y.; Asiri, A. M.; Yang, P. Synergistic Geometric and Electronic Effects for Electrochemical Reduction of Carbon Dioxide Using Gold−Copper Bimetallic Nanoparticles. *Nat. Commun.* **2014**, *5*, 4948.
(27) Andolina, C. M.; Dewar, A. C.; Smith, A. M.; Marbella, L. E.; Hartmann, M. J.; Millstone, J. E. Photoluminescent Gold−Copper Nanoparticle Alloys with Composition-Tunable near-Infrared Emission. *J. Am. Chem. Soc.* **2013**, *135*, 5266−5269.
(28) Motl, N. E.; Ewusi-Annan, E.; Sines, I. T.; Jensen, L.; Schaak, R. E. Au−Cu Alloy Nanoparticles with Tunable Compositions and Plasmonic Properties: Experimental Determination of Composition and Correlation with Theory. *J. Phys. Chem. C* **2010**, *114*, 19263−19269.
(29) Kamundi, M.; Bromberg, L.; Fey, E.; Mitchell, C.; Fayette, M.; Dimitrov, N. Impact of Structure and Composition on the Dealloying of $Au_xAg_{(1-x)}$ Alloys on the Nanoscale. *J. Phys. Chem. C* **2012**, *116*, 14123−14133.
(30) Strmcnik, D.; Tripkovic, D.; van der Vliet, D.; Stamenkovic, V.; Markovic, N. M. Adsorption of Hydrogen on Pt(111) and Pt(100) Surfaces and Its Role in the Hor. *Electrochem. Commun.* **2008**, *10*, 1602−1605.
(31) Herrero, E.; Clavilier, J.; Feliu, J. M.; Aldaz, A. Influence of the Geometry of the Hanging Meniscus Contact on the Hydrogen Oxidation Reaction on a Pt(111) Electrode in Sulphuric Acid. *J. Electroanal. Chem.* **1996**, *410*, 125−127.
(32) Sauerbrey, G. Verwendung Von Schwingquarzen Zur Wägung Dünner Schichten Und Zur Mikrowägung. *Eur. Phys. J. A* **1959**, *155*, 206−222.
(33) Santos, M. C.; Miwa, D. W.; Machado, S. A. S. Study of Anion Adsorption on Polycrystalline Pt by Electrochemical Quartz Crystal Microbalance. *Electrochem. Commun.* **2000**, *2*, 692−696.
(34) Fayette, M.; Liu, Y.; Bertrand, D.; Nutariya, J.; Vasiljevic, N.; Dimitrov, N. From Au to Pt Via Surface Limited Redox Replacement of Pb UPD in One-Cell Configuration. *Langmuir* **2011**, *27*, 5650−5658.
(35) Xu, D.; Bliznakov, S.; Liu, Z. P.; Fang, J. Y.; Dimitrov, N. Composition-Dependent Electrocatalytic Activity of Pt-Cu Nanocube Catalysts for Formic Acid Oxidation. *Angew. Chem., Int. Ed.* **2010**, *49*, 1282−1285.
(36) Wei, S. H.; Mbaye, A. A.; Ferreira, L. G.; Zunger, A. 1st-Principles Calculations of the Phase-Diagrams of Noble-Metals - Cu-Au, Cu-Ag, and Ag-Au. *Phys. Rev. B: Condens. Matter Mater. Phys.* **1987**, *36*, 4163−4185.
(37) Dursun, A.; Pugh, D. V.; Corcoran, S. G. A Steady-State Method for Determining the Dealloying Critical Potential. *Electrochem. Solid-State Lett.* **2003**, *6*, B32−B34.
(38) Sieradzki, K.; Dimitrov, N.; Movrin, D.; McCall, C.; Vasiljevic, N.; Erlebacher, J. The Dealloying Critical Potential. *J. Electrochem. Soc.* **2002**, *149*, B370−B377.
(39) Yang, R. Z.; Strasser, P.; Toney, M. F. Dealloying of Cu_3pt (111) Studied by Surface X-Ray Scattering. *J. Phys. Chem. C* **2011**, *115*, 9074−9080.
(40) Liu, Y.; Bliznakov, S.; Dimitrov, N. Factors Controlling the Less Noble Metal Retention in Nanoporous Structures Processed by Electrochemical Dealloying. *J. Electrochem. Soc.* **2010**, *157*, K168−K176.
(41) Masel, R. I. *Principles of Adsorptionm and Reaction on Solid Surfaces*; John Willey & Sons, Inc.: New York, 1996; pp 42−43.
(42) Aslanides, A.; Hayoun, M.; Pontikis, V. Atomic Structure of Low-Index and (11n) Surfaces in Ordered Cu_3Au. *Surf. Sci.* **1997**, *370*, L163−L167.
(43) Liang, D. F.; Zangari, G. Underpotential Co-Deposition of Au-Cu Alloys: Switching the Underpotentially Deposited Element by Selective Complexation. *Langmuir* **2014**, *30*, 2566−2570.
(44) Plieth, W. J. Electrochemical Properties of Small Clusters of Metal Atoms and Their Role in the Surface Enhanced Raman Scattering. *J. Phys. Chem.* **1982**, *86*, 3166−3170.
(45) Ivanova, O. S.; Zamborini, F. P. Size-Dependent Electrochemical Oxidation of Silver Nanoparticles. *J. Am. Chem. Soc.* **2010**, *132*, 70−72.
(46) Bromberg, L.; Fayette, M.; Martens, B.; Luo, Z. P.; Wang, Y.; Xu, D.; Zhang, J.; Fang, J.; Dimitrov, N. Catalytic Performance Comparison of Shape-Dependent Nanocrystals and Oriented Ultrathin Films of Pt_4Cu Alloy in the Formic Acid Oxidation Process. *Electrocatalysis* **2013**, *4*, 24−36.
(47) Gan, L.; Cui, C. H.; Rudi, S.; Strasser, P. Core-Shell and Nanoporous Particle Architectures and Their Effect on the Activity and Stability of Pt Orr Electrocatalysts. *Top. Catal.* **2014**, *57*, 236−244.

NOTE ADDED AFTER ASAP PUBLICATION

This paper was published to the Web on January 25, 2016, with an error in the TOC and abstract graphics. This was corrected in the version published to the Web on January 26, 2016.

DOI: 10.1021/acs.jpcc.5b11637
J. Phys. Chem. C 2016, 120, 2299−2308